

Bias-dependent impedance model for ionic polymer-metal composites

Yannick Kengne Fotsing and Xiaobo Tan

Citation: *J. Appl. Phys.* **111**, 124907 (2012); doi: 10.1063/1.4730339

View online: <http://dx.doi.org/10.1063/1.4730339>

View Table of Contents: <http://jap.aip.org/resource/1/JAPIAU/v111/i12>

Published by the [American Institute of Physics](#).

Related Articles

Nanomanipulation and nanofabrication with multi-probe scanning tunneling microscope: From individual atoms to nanowires

Rev. Sci. Instrum. **83**, 063704 (2012)

A novel driving principle by means of the parasitic motion of the microgripper and its preliminary application in the design of the linear actuator

Rev. Sci. Instrum. **83**, 055002 (2012)

Dynamic analysis of dielectric elastomer actuators

Appl. Phys. Lett. **100**, 112903 (2012)

Rotating turkeys and self-commutating artificial muscle motors

Appl. Phys. Lett. **100**, 074108 (2012)

Measurement of insulating and dielectric properties of acrylic elastomer membranes at high electric fields

J. Appl. Phys. **111**, 024904 (2012)

Additional information on *J. Appl. Phys.*

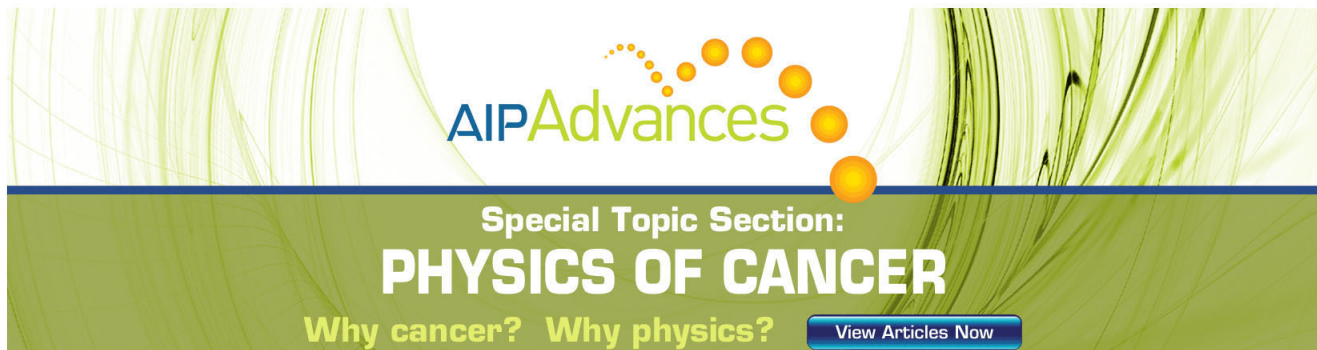
Journal Homepage: <http://jap.aip.org/>

Journal Information: http://jap.aip.org/about/about_the_journal

Top downloads: http://jap.aip.org/features/most_downloaded

Information for Authors: <http://jap.aip.org/authors>

ADVERTISEMENT

The advertisement features a green and yellow background with abstract wavy lines. At the top, the 'AIP Advances' logo is shown, with 'AIP' in blue and 'Advances' in green, accompanied by a series of orange dots. Below this, the text 'Special Topic Section: PHYSICS OF CANCER' is displayed in white, with 'PHYSICS OF CANCER' in a larger, bold font. At the bottom, the phrase 'Why cancer? Why physics?' is written in yellow, and a blue button with the text 'View Articles Now' is located on the right side.

AIP Advances

Special Topic Section:
PHYSICS OF CANCER

Why cancer? Why physics? [View Articles Now](#)

Bias-dependent impedance model for ionic polymer-metal composites

Yannick Kengne Fotsing^{a)} and Xiaobo Tan^{b)}

*Smart Microsystems Laboratory, Department of Electrical and Computer Engineering,
Michigan State University, East Lansing, Michigan 48824, USA*

(Received 2 July 2011; accepted 21 May 2012; published online 22 June 2012)

Ionic polymer-metal composites (IPMCs) are a novel class of soft sensing and actuation materials with promising applications in robotic and biomedical systems. In this paper, we present a model for nonlinear electrical dynamics of IPMC actuators, by applying perturbation analysis on the dynamics-governing partial differential equation (PDE) around a given bias voltage. By approximating the steady-state electric field under the bias with a piecewise linear function, we derive a linear PDE for the perturbed charge dynamics, which has piecewise constant coefficients and coefficients linear in the spatial variable. Through power series expansion, we solve the PDE to get the charge distribution up to any prescribed order. The perturbed electric field and current are subsequently obtained, which result in a bias-dependent impedance model. This model captures the nonlinear nature of the IPMC electrical dynamics and degenerates to the linear model when the bias is zero. The model predicts that, as the bias voltage increases, both the magnitude and the phase delay of the impedance decrease. These trends are quantitatively verified in experiments, where excellent agreement is achieved between the experimental measurements and model predictions. © 2012 American Institute of Physics. [<http://dx.doi.org/10.1063/1.4730339>]

I. INTRODUCTION

Ionic polymer-metal composites (IPMCs) are a novel class of soft actuation and sensing materials. An IPMC consists of three layers, with an ion-exchange polymer membrane (e.g., Nafion) sandwiched by metal electrodes. Inside the polymer, (negatively charged) anions covalently fixed to polymer chains are balanced by mobile (positively charged) cations. An applied voltage across an IPMC leads to the transport of cations and accompanying solvent molecules, resulting in both differential swelling and electrostatic forces inside the material, which cause the material to bend and hence the actuation effect.^{1,2} Because of their softness and low actuation voltage requirement, IPMC actuators have been proposed for various applications in biomedical devices and underwater robotics.^{3–6}

Recent years have seen significant advances in improving IPMC materials. One research thrust is on developing various electroding techniques to enhance actuation performance and electromechanical properties of IPMCs.^{7–10} Another research thrust is on understanding the roles of solvents and ions.^{11–13} For example, ionic fluids have been proposed as solvents for IPMCs to enable stable in-air actuation.^{14,15} Closely coupled with the material development effort is the interest in the modeling and understanding of IPMC actuation behavior and mechanisms.^{2,16–24} Current modeling work on IPMC actuators typically falls into three categories, with progressively increased level of complexity and fidelity: black-box models, gray-box models, and white-box models. Black-box models attempt to reproduce empirical responses without referring to the physical origin of the phenomena.^{25,26} These models are simple but are sample-dependent

and not geometrically scalable. The gray-box models incorporate some physical principles but still use empirical descriptions to define some other complex physical processes.^{27–29} White-box models, on the other hand, aim to capture the underlying physics of IPMC actuators.^{2,16,18–22,30–34}

A number of researchers have reported the characterization and modeling of nonlinear behaviors in IPMCs. For example, in the study of a linear, two-port transducer model for IPMCs, Newbury and Leo noted the significant impact of the initial curvature of an IPMC on its actuation response.³⁵ Bar-Cohen *et al.* reported the remanent deformation of an IPMC sample after the electrical activation was removed.³⁶ With a black-box approach, Bonomo and coworkers introduced diode elements into their circuit model to capture the nonlinear electrical response of IPMCs.²⁹ Hysteresis in IPMCs is another nonlinear phenomenon that has been studied by several groups. For example, Paquette *et al.* showed that a nanocomposite-IPMC exhibited less pronounced hysteresis in the current/voltage (I/V) characteristics than an untreated IPMC.³⁷ Chen and Tan proposed a black-box model for an IPMC actuator by cascading a Preisach hysteresis model with a linear system,³⁸ while Hao and Li used a parallel connection of a Prandtl-Ishlinskii model and linear dynamics to capture the hysteresis and creep behavior, respectively.³⁹ In addition, Kothera and Leo explored several tools in black-box nonlinear system identification, including Volterra series⁴⁰ and Hammerstein structures,⁴¹ to characterize and model nonlinear IPMC responses.

Most physics-based partial differential equation (PDE) models capture nonlinear dynamics in IPMCs, but typically, they can only be solved numerically and cannot be used for real-time control design. For example, Tadokoro *et al.* proposed a PDE model that accommodates electric field-induced ion transport, ion-dragged solvent transport, membrane swelling and contraction, and conformational changes and showed the

^{a)}Electronic mail: kengnefo@msu.edu.

^{b)}Electronic mail: xbtan@msu.edu.

agreement of simulation results with experimental measurement on the actuation response under a step voltage input.³¹ Wallmersperger *et al.* developed a model of transport and electromechanical transduction based upon a coupled chemoelectrical multifield formulation and employed an adaptive multigrid method to obtain the numerical resolution, which was found to match the experimental results.⁴² While these models are instrumental in understanding the physics of IPMCs, they rely on numerical solutions and offer little direct analytical insight. On the other hand, several methods have been explored by researchers to gain certain analytical insight into nonlinear IPMC behaviors (especially electrical behaviors) from physics-based models. For example, Porfiri proposed Poisson–Nernst–Planck equations to model the time evolution of the electric potential and the concentration of mobile cations and used the method of matched asymptotic expansions to compute the nonlinear capacitance of an IPMC and consequently derived a physics-based circuit model.²² Davidson and Goulbourne also applied the matched asymptotic expansions method to study the capacitance of ionic liquid-based IPMCs.⁴³ Nonlinear capacitance of an IPMC has also been developing by Chen *et al.*⁴⁴ by deriving the steady-state solution under a step voltage, for the nonlinear dynamics-governing PDE.² While all these works shed important light on the nonlinear capacitance, they do not provide closed-form dynamic models for IPMCs. Finally, by dropping the nonlinear term in the governing PDE, Chen and Tan derived an explicit, infinite-dimensional transfer function model for the impedance and actuation behavior of IPMCs;⁴⁵ however, the linearity assumption implies that this model is only valid when the actuation voltage is low.

In this paper, we propose a new approach to the understanding of nonlinear IPMC electrical dynamics using perturbation analysis, which will result in closed-form transfer function models for IPMC impedance under different actuation voltage biases. In particular, the perturbed dynamics of an IPMC biased at any given voltage is examined. By approximating the steady-state electric field under the bias with a piecewise linear function, we derive a linear PDE for the perturbed charge dynamics, which has piecewise-constant coefficients and coefficients linear in the spatial variable. The latter coefficients depend on the bias voltage. Through power series expansion, we solve the PDE to get the charge distribution up to any prescribed order. The perturbed electric field and current are subsequently obtained, yielding a bias-dependent impedance model. This model captures the nonlinear nature of the IPMC electrical dynamics and degenerates to the linear model when the bias is zero. The impedance model predicts that, as the bias voltage increases, both the magnitude and the phase delay of the impedance decrease. Experiments on an IPMC sample have been conducted to characterize its electrical behavior under four different biases from 0 to 1.5 V. Experimental results have quantitatively confirmed the model-predicted trends.

To our best knowledge, this work is the first to formally report the bias-dependent impedance of IPMCs and to provide a theoretical explanation. The proposed model is also expected to be instrumental in control design for IPMC actuators.

The remainder of the paper is organized as follows. We first present the analysis and piecewise-linear approximation of the electric field under a constant voltage (bias) in Sec. II. The perturbation analysis is presented in Sec. III, to derive the bias-dependent impedance model. Methods and materials for experimental model validation are described in Sec. IV, and the results are presented and discussed in Sec. V. Finally, concluding remarks are provided in Sec. VI.

II. STEADY-STATE FIELD ANALYSIS AND APPROXIMATION

We first analyze the steady-state distribution of the electric field within the polymer when a bias voltage is applied. Numerical results indicate that the field can be approximated with a piecewise linear function that has three segments. The later perturbation analysis will be performed around this approximate steady-state field distribution.

A. Review of dynamics-governing PDEs

We start with the PDE model for ion transport dynamics that was originally proposed by Nemat-Nasser and Li.² Consider Fig. 1, where an IPMC beam is clamped at one end ($z=0$) and its displacement at the other end ($z=L$) is denoted by $w(t)$. The neutral axis of the beam is denoted by $x=0$, and the upper and lower surfaces are denoted by $x=h$ and $x=-h$, respectively.

Typically, the lateral dimensions of an IPMC beam are much greater than its thickness, which allows us to assume that all field variables (electric field, electric displacement, etc.) inside the polymer are restricted to the thickness direction only. Let ϕ , E , D , and ρ denote the electric potential, electric field, electric displacement, and the charge density, respectively. The following equations hold as:

$$E = \frac{D}{\kappa_e} = \frac{\partial \phi}{\partial x}, \quad (1)$$

$$\rho = \frac{\partial D}{\partial x} = F(C^+ - C^-), \quad (2)$$

where κ_e is the effective dielectric constant of the polymer, F is the Faraday's constant, and C^+ and C^- are the cation and anion concentrations, respectively.

Using the continuity equation, we get

$$\frac{\partial J}{\partial x} = -\frac{\partial C^+}{\partial t}. \quad (3)$$

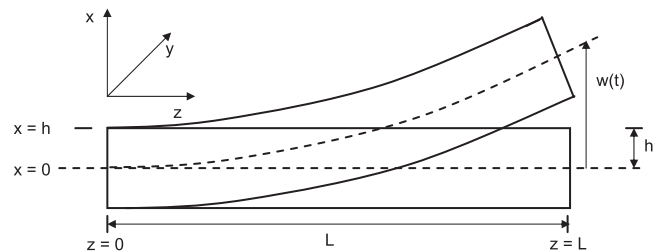


FIG. 1. Geometric definition of an IPMC cantilever beam.

The ion flux consists of diffusion, migration, and convection terms, and can be derived as²

$$J = -\frac{d\kappa_e}{F} \left(\frac{\partial^2 E}{\partial x^2} - \frac{F(1 - C^-\delta_V)}{RT} E \left(\frac{\partial E}{\partial x} + \frac{FC^-}{\kappa_e} \right) \right), \quad (4)$$

where d is the ionic diffusivity, R is the gas constant, T is the absolute temperature, and δ_V is the volumetric change, which represents how much the polymer volume swells after taking water. With Eq. (3), one can derive the nonlinear PDE in terms of the electric field as

$$\frac{\partial^2 E}{\partial x \partial t} = d \left(\frac{\partial^3 E}{\partial x^3} - \frac{F(1 - C^-\delta_V)}{RT} \left[\frac{\partial^2 E}{\partial x^2} E + \left(\frac{\partial E}{\partial x} \right)^2 \right] - \frac{F^2 C^- (1 - C^-\delta_V)}{RT \kappa_e} \frac{\partial E}{\partial x} \right). \quad (5)$$

In several papers,^{2,16,32,45} the nonlinear term involving in Eq. (5) has been dropped based on the assumption

$$\rho(x) = \kappa_e \frac{\partial E}{\partial x} \ll C^- F, \quad (6)$$

resulting in a linear PDE, which has been used to derive closed-form models for IPMC dynamics.^{32,45} However, Chen and Tan⁴⁴ show that the assumption (6) holds only for small actuation voltages (<0.2 V). The goal of this paper, therefore, is to develop closed-form models that are valid independent of the assumption (6).

B. Steady-state field distribution under a constant voltage

We first analyze the steady-state charge and electric field distributions under a constant applied voltage V_0 . This will be instrumental in our perturbation analysis later. Under a constant voltage, the system will approach the equilibrium state, where $J = 0$. Equation (4) then implies

$$\frac{\partial^2 E_0}{\partial x^2} - \frac{F(1 - C^-\delta_V)}{RT} E_0 \left(\frac{\partial E_0}{\partial x} + \frac{FC^-}{\kappa_e} \right) = 0, \quad (7)$$

where E_0 represents the steady-state distribution of the electric field. Two additional equations are required for solving for E_0 and the corresponding charge distribution ρ_0 :

- (1) The overall charge-balance condition leads to

$$\int_{-h}^h \rho_0(x) dx = 0, \quad (8)$$

where $\rho_0 = \kappa_e \frac{\partial E_0}{\partial x}$.

- (2) The potential difference across IPMC is equal to the applied voltage

$$\int_{-h}^h E_0(x) dx = V_0. \quad (9)$$

Chen and Tan⁴⁴ proposed a recursive scheme for numerically solving Eqs. (7)–(9). We have adopted the same

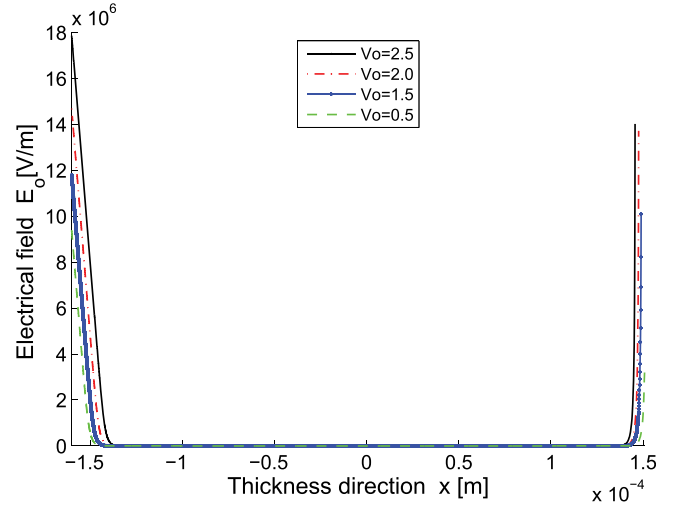


FIG. 2. Simulation results: steady-state electric field distribution under constant voltages.

scheme to solve for the field distributions under different voltages (Fig. 2). Table I lists the parameters used in our computation, which were identified for an IPMC sample used in the experiments of this work. Following Nemat-Nasser and Li,² we take $1 - C^-\delta_V \approx 1$. From Fig. 2, under each voltage, the electric field vanishes except in the boundary regions. Furthermore, as the voltage V_0 increases, both the electric field value and the range of its non-vanishing region increase.

Another observation one can make from Fig. 2 is that the electric field in the boundary regions varies with the spatial variable x in a linear fashion, at least to the first-order approximation. We thus propose the approximation of the field distribution with a piecewise linear function, which will greatly facilitate the model development later on. In particular, we approximate E_0 as

$$E_0(x) = \begin{cases} E_{0,1} = a_1 x + b_1, & \text{for } x < h_1 \\ E_{0,2} = a_2 x + b_2, & \text{for } h_1 \leq x \leq h_2 \\ E_{0,3} = a_3 x + b_3, & \text{for } x > h_2 \end{cases} \quad (10)$$

where $h_1 = -\frac{b_1}{a_1}$ and $h_2 = -\frac{b_3}{a_3}$ denote the approximate boundaries for the zero-field region, and $a_2 = b_2 = 0$. Fig. 3 illustrates the piecewise-linear approximation for the case of $V_0 = 1.5$ V, and Table II lists the approximating coefficients $a_i, b_i, i = 1, 2, 3$, for all cases computed in Fig. 2.

III. BIAS-DEPENDENT IMPEDANCE MODEL

A. Perturbation analysis

The nonlinear PDE (5) can be compactly written as

TABLE I. Parameters used in numerical solving Eqs. (7)–(9).

F C/mol	R C/(mol·K)	T K	κ_e F/m	C^- mol/m ³	h m
9.6485×10^4	8.31	300	2.43×10^{-5}	1091	1.6×10^{-4}

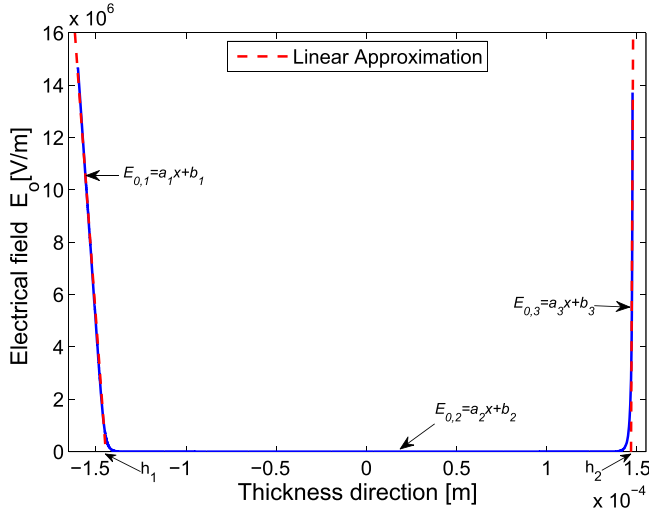


FIG. 3. Piecewise-linear approximation of the steady state electric field for $V_0 = 1.5$ V.

$$\frac{\partial^2 E}{\partial x \partial t} = d \left(\frac{\partial^3 E}{\partial x^3} - f \left[\frac{\partial^2 E}{\partial x^2} E + \left(\frac{\partial E}{\partial x} \right)^2 \right] - g \frac{\partial E}{\partial x} \right), \quad (11)$$

where f and g are constants given by

$$f \triangleq \frac{F(1 - C^- \delta_V)}{RT} \quad \text{and} \quad g \triangleq \frac{F^2 C^- (1 - C^- \delta_V)}{RT \kappa_e}. \quad (12)$$

We now consider applying a voltage input V that is perturbed from a constant bias V_0 ,

$$V(t) = V_0 + \epsilon V_1(t), \quad (13)$$

where $0 < \epsilon \ll 1$. The solution to Eq. (11), $\bar{E}(x, t, \epsilon)$, can be expanded around $\epsilon = 0$

$$\bar{E}(x, t, \epsilon) = E_0(x) + \epsilon E_1(x) + \epsilon^2 E_2(x) + \dots,$$

where $E_0(x)$ represents the steady-state field distribution under the bias voltage V_0 . For perturbation analysis, we ignore terms involving ϵ^2 and higher order terms and obtain an approximate solution of the form

$$E(x, t) = E_0(x) + \epsilon E_1(x, t). \quad (14)$$

We plug Eq. (14) into each term in Eq. (11) and ignore terms involving ϵ^2 ,

TABLE II. Coefficients for piecewise-linear approximation of the electric field, for $V_0 = 0.5, 1.5, 2.0, 2.5$ V.

	a_1	b_1	a_2	b_2	a_3	b_3
$V_0 = 0.5$	-8.68×10^{11}	-1.30×10^8	0	0	2.01×10^{12}	-2.99×10^8
$V_0 = 1.5$	-9.31×10^{11}	-1.37×10^8	0	0	2.64×10^{12}	-3.88×10^8
$V_0 = 2.0$	-9.53×10^{11}	-1.38×10^8	0	0	4.55×10^{12}	-6.64×10^8
$V_0 = 2.5$	-9.65×10^{11}	-1.37×10^8	0	0	4.87×10^{12}	-7.01×10^8

$$\begin{aligned} \frac{\partial E}{\partial x} &= \frac{\partial E_0}{\partial x} + \epsilon \frac{\partial E_1}{\partial x} \\ \frac{\partial^2 E}{\partial x \partial t} &= \epsilon \frac{\partial^2 E_1}{\partial x \partial t} \\ \left(\frac{\partial E}{\partial x} \right)^2 &= \left(\frac{\partial E_0}{\partial x} + \epsilon \frac{\partial E_1}{\partial x} \right)^2 \\ &= \left(\frac{\partial E_0}{\partial x} \right)^2 + 2\epsilon \frac{\partial E_0}{\partial x} \frac{\partial E_1}{\partial x} + \epsilon^2 \left(\frac{\partial E_1}{\partial x} \right)^2 \\ \frac{\partial^2 E}{\partial x^2} E &= \left(\frac{\partial^2 E_0}{\partial x^2} + \epsilon \frac{\partial^2 E_1}{\partial x^2} \right) (E_0 + \epsilon E_1) \\ &= \frac{\partial^2 E_0}{\partial x^2} E_0 + \epsilon \frac{\partial^2 E_0}{\partial x^2} E_1 + \epsilon \frac{\partial^2 E_1}{\partial x^2} E_0 + \epsilon^2 \frac{\partial^2 E_1}{\partial x^2} E_1 \\ \frac{\partial^3 E}{\partial x^3} &= \frac{\partial^3 E_0}{\partial x^3} + \epsilon \frac{\partial^3 E_1}{\partial x^3}. \end{aligned}$$

Equation (11) is then rewritten as

$$\begin{aligned} \epsilon \frac{\partial^2 E_1}{\partial x \partial t} &= \frac{\partial^3 E_0}{\partial x^3} + \epsilon \frac{\partial^3 E_1}{\partial x^3} - f \left[\frac{\partial^2 E_0}{\partial x^2} E_0 + \epsilon \frac{\partial^2 E_0}{\partial x^2} E_1 \right. \\ &\quad \left. + \epsilon \frac{\partial^2 E_1}{\partial x^2} E_0 + \left(\frac{\partial E_0}{\partial x} \right)^2 + 2\epsilon \frac{\partial E_0}{\partial x} \frac{\partial E_1}{\partial x} \right] \\ &\quad - g \left(\frac{\partial E_0}{\partial x} + \epsilon \frac{\partial E_1}{\partial x} \right). \end{aligned} \quad (15)$$

From Eq. (7), we have

$$\frac{\partial^3 E_0}{\partial x^3} - f \left(\frac{\partial^2 E_0}{\partial x^2} E_0 + \left(\frac{\partial E_0}{\partial x} \right)^2 \right) - g \frac{\partial E_0}{\partial x} = 0, \quad (16)$$

which allows us to simplify Eq. (15) to

$$\begin{aligned} \frac{1}{d} \frac{\partial^2 E_1}{\partial x \partial t} &= \frac{\partial^3 E_1}{\partial x^3} - f \left[\frac{\partial^2 E_0}{\partial x^2} E_1 + E_0 \frac{\partial^2 E_1}{\partial x^2} + 2 \frac{\partial E_0}{\partial x} \frac{\partial E_1}{\partial x} \right] \\ &\quad - g \frac{\partial E_1}{\partial x}. \end{aligned} \quad (17)$$

The charge density $\rho(x, t)$ can be decomposed as

$$\rho(x, t) = \rho_0(x) + \epsilon \rho_1(x, t), \quad (18)$$

where $\rho_1 = \kappa_e \frac{\partial E_1}{\partial x}$. Equation (17) can be rewritten in terms of ρ_1 ,

$$\begin{aligned} \frac{1}{d} \frac{\partial \rho_1}{\partial t} - \frac{\partial^2 \rho_1}{\partial x^2} + f \kappa_e \frac{\partial^2 E_0}{\partial x^2} E_1 + f \frac{\partial \rho_1}{\partial x} E_0 \\ + 2f \frac{\partial E_0}{\partial x} \rho_1 + g \rho_1 = 0. \end{aligned} \quad (19)$$

With the piecewise-linear approximation (10) for $E_0(x)$, we have $\frac{\partial^2 E_0}{\partial x^2} = 0$ for all x except at $x = h_1, h_2$, and $\frac{\partial E_0}{\partial x} = a_i$, where $a_i, i = 1, 2, 3$, is as defined in Eq. (10). The PDE (19) for ρ_1 can then be simplified as

$$\frac{1}{d} \frac{\partial \rho_1}{\partial t} - \frac{\partial^2 \rho_1}{\partial x^2} + f \frac{\partial \rho_1}{\partial x} E_0 + 2f a_i \rho_1 + g \rho_1 = 0, \quad (20)$$

which can be further converted to the Laplace domain

$$-\frac{\partial^2 \rho_1}{\partial x^2} + f(a_i x + b_i) \frac{\partial \rho_1}{\partial x} + \left(\frac{s}{d} + 2aif + g\right) \rho_1 = 0, \quad (21)$$

where s is the Laplace variable, and with a bit abuse of notation, $\rho_1 = \rho_1(x, s)$ now represents the charge distribution in the s -domain. For ease of presentation, we will also use the same notation to represent E_1 and V_1 in the time- and s -domains.

B. Derivation of the impedance model

The charge density ρ_1 can be solved from Eq. (21) together with the following two conditions:

$$\int_{-h}^h \rho_1(x, s) dx = 0, \quad (22)$$

$$\int_{-h}^h E_1(x, s) dx = \frac{1}{\kappa_e} \int_{-h}^h \int_0^x \rho_1(\xi, s) d\xi dx = V_1(s). \quad (23)$$

Note that in the first equality in Eq. (23) we have used the observation $E_1(0, s) \approx 0$.

Some of the coefficients in Eq. (21) are piecewise constant and some have x -dependence, which prevents one from obtaining a closed-form solution. Instead, we represent ρ_1 with a power series, the coefficients of which depend on x ,

$$\rho_1(x, s) = \sum_{n=0}^{\infty} \alpha_{n,i}(s) x^n, \quad (24)$$

where

$$i = \begin{cases} 1, & \text{if } x < h_1 \\ 2, & \text{if } h_1 \leq x \leq h_2 \\ 3, & \text{if } x > h_2 \end{cases} \quad (25)$$

Subsequently, we have

$$\frac{\partial \rho_1}{\partial x} = \sum_{n=1}^{\infty} n \alpha_{n,i}(s) x^{n-1}, \quad (26)$$

$$\frac{\partial^2 \rho_1}{\partial x^2} = \sum_{n=2}^{\infty} n(n-1) \alpha_{n,i}(s) x^{n-2}. \quad (27)$$

Plugging Eqs. (25)–(27) into Eq. (21), we have

$$-\sum_{n=2}^{\infty} n(n-1) \alpha_{n,i} x^{n-2} + aif \sum_{n=1}^{\infty} n \alpha_{n,i} x^n + fb_i \sum_{n=1}^{\infty} n \alpha_{n,i} x^{n-1} + \left(\frac{s}{d} + 2aif + g\right) \sum_{n=0}^{\infty} \alpha_{n,i} x^n = 0. \quad (28)$$

Equation (28) can be manipulated into the following form:

$$-\sum_{n=0}^{\infty} (n+2)(n+1) \alpha_{n+2,i} x^n + aif \sum_{n=1}^{\infty} n \alpha_{n,i} x^n + fb_i \sum_{n=0}^{\infty} (n+1) \alpha_{n+1,i} x^n + \left(\frac{s}{d} + 2aif + g\right) \sum_{n=0}^{\infty} \alpha_{n,i} x^n = 0.$$

Equating the coefficients of powers of x , we obtain, for $n=0$,

$$-2\alpha_{2,i} + fb_i \alpha_{1,i} + \left(\frac{s}{d} + 2aif + g\right) \alpha_{0,i} = 0, \quad (29)$$

and for $n \geq 1$,

$$-(n+2)(n+1) \alpha_{n+2,i} + aif n \alpha_{n,i} + fb_i (n+1) \alpha_{n+1,i} + \left(\frac{s}{d} + 2aif + g\right) \alpha_{n,i} = 0. \quad (30)$$

Equations (29) and (30) imply, for all $n \geq 0$,

$$\alpha_{n+2,i} = \frac{fb_i (n+1) \alpha_{n+1,i} + \left(\frac{s}{d} + aif(n+2) + g\right) \alpha_{n,i}}{(n+2)(n+1)}. \quad (31)$$

With the recursion (31), one can express all coefficients $\alpha_{n,i}$, $n \geq 2$, in terms of $\alpha_{0,i}$ and $\alpha_{1,i}$, and we can obtain the latter by using Eqs. (22) and (23). It turns out that $\alpha_{0,i}$ and $\alpha_{1,i}$ are independent of i and we will simply write them as α_0 and α_1 , respectively. In practice, we seek an approximation to the power series (24)

$$\rho_1(x, s) = \sum_{n=0}^N \alpha_{n,i} x^n = \alpha_0 + \alpha_1 x + \alpha_{2,i} x^2 + \cdots + \alpha_{N,i} x^N, \quad (32)$$

for a given N .

Once $\rho_1(x, s)$ is obtained, we can evaluate the transferred charge $Q_1(s)$ and the current $I_1(s)$ associated with the applied voltage $V_1(s)$,

$$Q_1(s) = A \int_0^h \rho_1(x, s) dx, \\ I_1(s) = sQ_1(s),$$

where A is the surface area of the IPMC. The bias-dependent impedance model, for a given order N , is then derived as

$$Z(s) = \frac{V_1(s)}{I_1(s)} = \frac{\tilde{a}_{N-1} s^{N-1} + \cdots + \tilde{a}_2 s^2 + \tilde{a}_1 s + \tilde{a}_0}{s(\tilde{b}_{N-1} s^{N-1} + \cdots + \tilde{b}_2 s^2 + \tilde{b}_1 s + \tilde{b}_0)}, \quad (33)$$

where $\tilde{a}_0, \tilde{a}_1, \dots, \tilde{a}_{N-1}$ and $\tilde{b}_0, \tilde{b}_1, \dots, \tilde{b}_{N-1}$ are constants that are dependent on the physical parameters of the IPMC. For example, for $N=1$,

$$Z(s) = -\frac{2h}{s(3A\kappa_e)}.$$

Note that when the bias $V_0=0$, the steady-state electric field $E_0(x) \equiv 0$, and thus $a_i = b_i = 0$, for $i \in \{1, 2, 3\}$. In this case, the PDE (21) for the charge distribution degenerates to the one obtained by dropping the nonlinear term in Eq. (5), and thus the resulting impedance model becomes the same as the linear model derived by Chen and Tan⁴⁵ (when the surface resistance of the IPMC is ignored). Therefore, our model encompasses the linear model as a special case.

IV. EXPERIMENTAL MODEL VERIFICATION: MATERIALS AND METHODS

A. Material and experimental setup

Experiments were conducted on an IPMC sample, obtained from Environmental Robots, Inc., to validate the proposed bias-dependent impedance model. The sample was Nafion-based with platinum electrodes. We post-processed the sample by depositing a $0.5\ \mu\text{m}$ thick layer of gold on each electrode surface to enhance its conductivity. This resulted in negligible surface resistance, thus satisfying the assumption made in the modeling work. The sample was 51 mm long, 11 mm wide, and $320\ \mu\text{m}$ thick. The free length of the sample was 47 mm in the cantilevered configuration. All experiments were conducted at room temperature.

In experiments, the cantilevered IPMC beam was soaked in deionized water. For verification of the impedance models, actuation voltages of the form $V_0 + 0.2 \sin(\omega t)$ V were applied. Four different values of the bias V_0 were used, 0 V, 0.5 V, 1 V, and 1.5 V. For each bias value, AC actuation voltages ranging 0.1–100 Hz were used for measuring the corresponding impedance responses. The actuation signals were generated from a computer equipped with a dSPACE system (DS 1104 R&D Controller Board and Control Desk, dSPACE) and amplified by a power amplifier (BOP 36–6D, Kepco) before being applied to the IPMC. The actuation voltage and current signals were captured by the dSPACE system. Fast Fourier transforms were performed on these signals in MATLAB to extract the magnitude and phase at any given frequency, from which the empirical gain and phase frequency responses were obtained and used for the model validation.

B. Methods for parameter identification

Faraday's constant F and the gas constant R are physical constants and thus do not require identification: $F = 9.6487 \times 10^4\ \text{C/mol}$, $R = 8.31\ \text{J/(mol}\cdot\text{K)}$. The sample dimensions were measured directly; in particular, the half thickness $h = 1.6 \times 10^{-4}\ \text{m}$. The absolute temperature T was taken to be 300 K. The volumetric change δ_V was set to be zero,² and the anion concentration C^- was taken to be $1091\ \text{mol/m}^3$ following the reported values in the literature.⁴⁵

The remaining parameters for the impedance model include the ionic diffusivity d and the effective dielectric constant κ_e . These two parameters were determined with data fitting. This process, however, was not straightforward because the coefficients $\{a_i, b_i\}_{i=1}^3$ in Eq. (21) and thus Eq. (33) depends on the numerically computed field profile $E_0(x)$, and the computation of $E_0(x)$ requires knowing the parameters including κ_e . A recursive procedure was taken to solve this problem. We started with reported values for d and κ_e in the literature,^{44,45} ran simulation for the steady-state equations (7)–(9) and obtained $\{a_i, b_i\}_{i=1}^3$. We then used the MATLAB function *lsqnonlin* to identify d and κ_e to minimize the error between the model predictions and the experimental data on the impedance spectrum. With the newly obtained value for κ_e , we went back to recompute E_0 and $\{a_i, b_i\}_{i=1}^3$. This process was repeated until the best data fit was achieved. Note that although these two parameters were identified

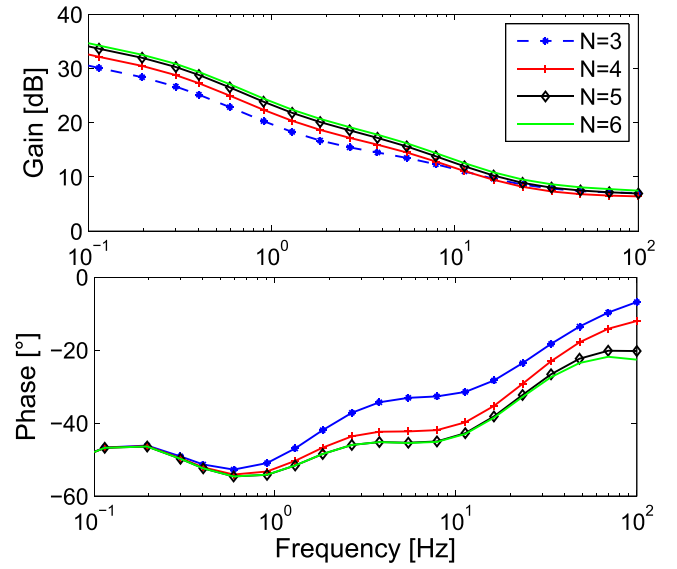


FIG. 4. Convergence of the impedance model as the order N increases. The bias voltage $V_0 = 1.5$ V.

through data fitting, the simultaneous matching of four data sets (as described in Sec. V), each including gain and phase responses at multiple frequencies, provides adequate evidence supporting the modeling approach itself.

V. RESULTS AND DISCUSSIONS

The impedance model (33) contains an order parameter N . The model is expected to be more accurate with larger N , but a larger N implies higher complexity. Therefore, a suitable N needs to be determined. Fig. 4 shows the evolution of the impedance spectrum as the order N of the approximating power series for ρ_1 is increased, where the bias voltage V_0 is 1.5 V. We can see that the approximating series converges and $N = 6$ provides adequate accuracy in the approximation. This value of N is used in all model predictions presented in this section.

Fig. 5 shows the measured impedance spectra of the IPMC sample under four different biases, $V_0 = 0, 0.5, 1, 1.5$ V.

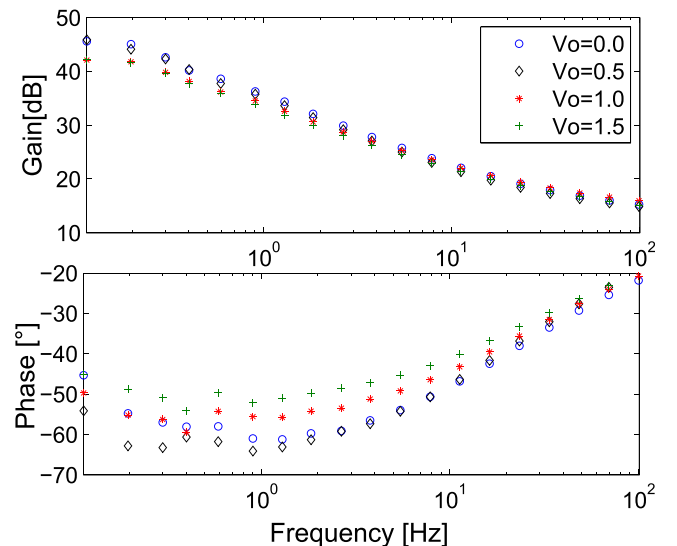


FIG. 5. Measured IPMC impedance spectra for the bias $V_0 = 0.0, 0.5, 1.0, 1.5$ V.

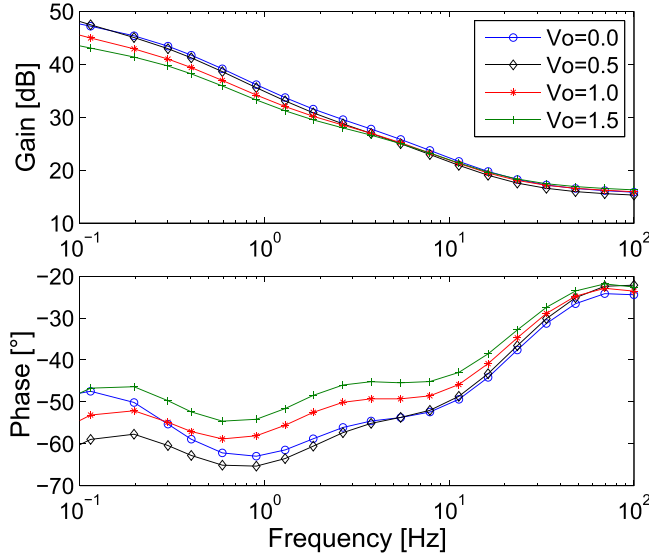


FIG. 6. Model predictions of IPMC impedance spectra for the bias $V_0 = 0, 0.5, 1.0, 1.5$ V.

It can be observed that within the tested frequency range of 0.1–100 Hz, the gain response decreases (implying higher current response) with the frequency, while the phase lead between the current and the voltage (negative of the shown phase) initially increases and then drops with the frequency. In addition, as the bias increases, the gain response decreases (higher current response), while the phase lead between the current and the voltage drops. Fig. 6 shows the model predictions of the impedance spectra under the same set of bias voltages. We can see that the model predictions not only capture the trends of gain and phase responses as the frequency increases but also capture the trends when the bias increases. To provide a closer comparison between the model and the experimental data, we put the model prediction and experimental measurement for each bias on the same graph; see Figs. 7–10. The good agreement in all cases provides strong

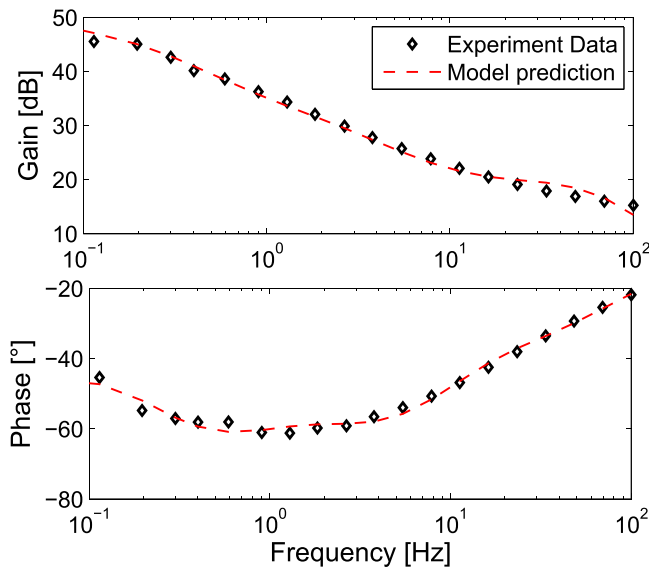


FIG. 7. Model prediction versus experimental measurement of the IPMC impedance spectrum when the bias $V_0 = 0.0$ V.

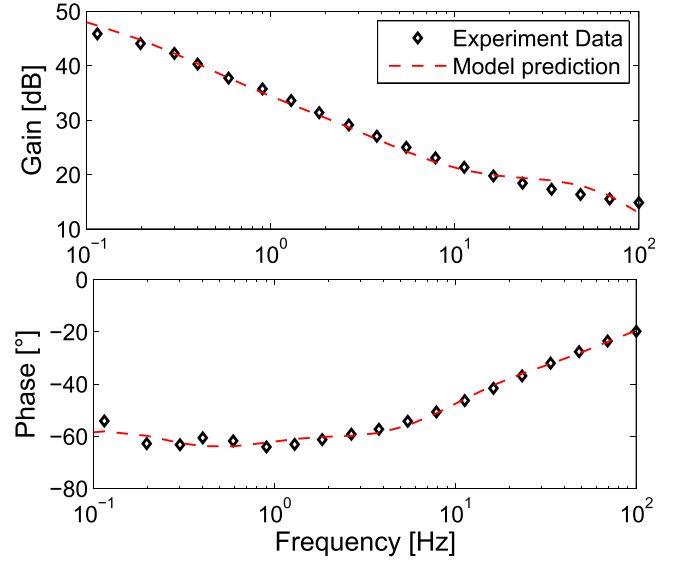


FIG. 8. Model prediction versus experimental measurement of the IPMC impedance spectrum when the bias $V_0 = 0.5$ V.

evidence that the model is able to capture the bias-dependent impedance of IPMC materials. Note that, as we commented at the end of Sec. III, the bias-dependent impedance model for the case of $v_0 = 0$ V coincides with the linear model. Therefore, from Figs. 5–10, while the linear model is able to provide a good prediction for the zero-DC bias case, it will fail to capture the impedance changes as the DC bias is increased.

While one would expect that the impedance spectrum varies monotonically with the bias, one exception can be found for the phase response. In particular, as seen in Fig. 5, the phase response under zero bias ($V_0 = 0$ V) within the low frequency range (<10 Hz) is not consistent with the bias-dependent trend observed for the other curves; it would have fallen under the phase response for $V_0 = 0.5$ V if following the trend. While we do not have an intuitive explanation for

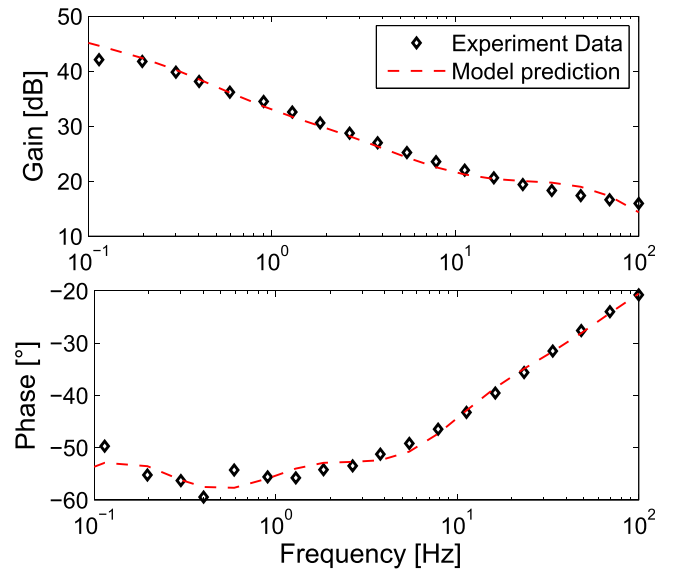


FIG. 9. Model prediction versus experimental measurement of the IPMC impedance spectrum when the bias $V_0 = 1.0$ V.

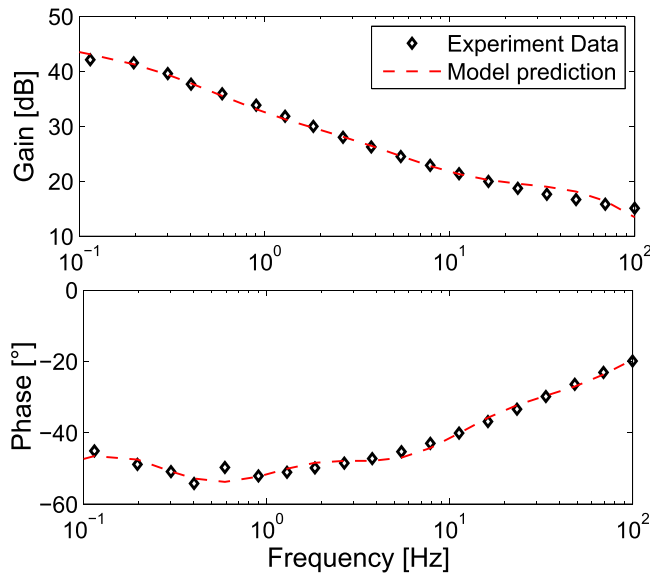


FIG. 10. Model prediction versus experimental measurement of the IPMC impedance spectrum when the bias $V_0 = 1.5$ V.

this phenomenon at this moment, the model prediction in Fig. 6 actually captures this “exception” precisely.

VI. CONCLUSION AND FUTURE WORK

In this paper, we reported for the first time the dependence of the electrical dynamics of IPMCs on the bias actuation voltage and presented rigorous modeling analysis for this phenomenon. The proposed model started with the nonlinear PDE governing the charge dynamics. Instead of directly dropping the nonlinear term in the PDE, we performed perturbation analysis around a given operating point characterized by a constant bias. The methodology for solving the resulting PDE for the perturbed dynamics was developed, with which closed-form local impedance models were derived. The proposed bias-dependent impedance model was validated experimentally.

There are several directions in which this work can be extended. In this paper, we have assumed perfectly conducting electrode surfaces. It is of interest to incorporate the effect of surface resistance into the model, as done by Chen and Tan⁴⁵ in the development of a linear, physics-based model. Second, we are interested in characterizing and modeling the dependence of the actuation dynamics on the bias voltage. A natural model structure for the actuation dynamics comprises a cascading of electrical dynamics, electromechanical coupling, and mechanical dynamics.^{4,45} In addition to the bias-dependent electrical dynamics as studied in this paper, the mechanical dynamics will also exhibit bias-dependent nonlinear behavior for two reasons. An applied bias voltage induces compressive stress and tensile stress on the anode and cathode sides of the IPMC, respectively. Due to the stress-stiffening effect,^{46,47} the apparent stiffness and thus the natural frequencies of the IPMC beam will be bias-dependent. Moreover, with the large deformation induced by a relatively large bias voltage, linear stress-strain relationship no longer applies and one will need to incorporate nonlinear mechanics into the modeling process.⁴⁸ We will investigate

how to accommodate both stress-stiffening and large-deformation effects in modeling the bias-dependent mechanical dynamics, which will then be used to construct the full actuation model.

ACKNOWLEDGMENTS

This work was supported in part by NSF (ECCS 0547131, IIS 0916720) and ONR (Grant No. N000140810640, program manager Dr. T. McKenna). The authors wish to thank Hong Lei for preparing the IPMC material and fine-tuning the experimental setup.

- ¹M. Shahinpoor and K. Kim, *Smart Mater. Struct.* **10**, 819 (2001).
- ²S. Nemat-Nasser and J. Li, *J. Appl. Phys.* **87**, 3321 (2000).
- ³M. Shahinpoor and K. Kim, *Smart Mater. Struct.* **14**, 197 (2005).
- ⁴Z. Chen, S. Shatara, and X. Tan, *IEEE/ASME Trans. Mechatron.* **15**, 448 (2010).
- ⁵S. D. Peterson, M. Porfiri, and A. Rovardi, *IEEE/ASME Trans. Mechatron.* **14**, 474 (2009).
- ⁶M. Aureli, V. Kopman, and M. Porfiri, *IEEE/ASME Trans. Mechatron.* **15**, 603 (2010).
- ⁷D. Y. Lee, I.-S. Park, M.-H. Lee, K. J. Kim, and S. Heo, *Sens. Actuators, A* **133**, 117 (2007).
- ⁸S.-M. Kim and K. Kim, *Smart Mater. Struct.* **17**, 035011 (2008).
- ⁹B. J. Akle, W. Habchi, T. Wallmersperger, E. J. Akle, and D. J. Leo, *J. Appl. Phys.* **109**, 074509 (2011).
- ¹⁰R. Montazami, S. Liu, Y. Liu, D. Wang, Q. Zhang, and J. R. Heflin, *J. Appl. Phys.* **109**, 104301 (2011).
- ¹¹S. Nemat-Nasser and Y. Wu, *J. Appl. Phys.* **93**, 5255 (2003).
- ¹²S. Nemat-Nasser, S. Zamani, and Y. Tor, *J. Appl. Phys.* **99**, 104902 (2006).
- ¹³K. Kikuchi, T. Sakamoto, S. Tsuchitani, and K. Asaka, *J. Appl. Phys.* **109**, 073505 (2011).
- ¹⁴B. J. Akle, M. D. Bennett, and D. J. Leo, *Sens. Actuators, A* **126**, 173 (2006).
- ¹⁵K. Kikuchi and S. Tsuchitani, *J. Appl. Phys.* **106**, 053519 (2009).
- ¹⁶S. Nemat-Nasser, *J. Appl. Phys.* **92**, 2899 (2002).
- ¹⁷H. Tamagawa, K. Yagasaki, and F. Nogata, *J. Appl. Phys.* **92**, 7614 (2002).
- ¹⁸L. Weiland and D. Leo, *J. Appl. Phys.* **97**, 013541 (2005).
- ¹⁹L. Weiland and D. Leo, *J. Appl. Phys.* **97**, 123530 (2005).
- ²⁰S. Nemat-Nasser and S. Zamani, *J. Appl. Phys.* **100**, 064310 (2006).
- ²¹D. Pugal, K. J. Kim, A. Punning, H. Kasemagi, M. Kruusmaa, and A. Aabloo, *J. Appl. Phys.* **103**, 084908 (2008).
- ²²M. Porfiri, *J. Appl. Phys.* **104**, 104915 (2008).
- ²³M. Aureli, W. Lin, and M. Porfiri, *J. Appl. Phys.* **104**, 104911 (2009).
- ²⁴I.-S. Park, S.-M. Kim, D. Pugal, L. Huang, S.-W. Tam-Chang, and K. J. Kim, *Appl. Phys. Lett.* **96**, 043301 (2010).
- ²⁵R. Kanno, A. Kurata, S. Tadokoro, T. Takamori, and K. Oguro, in *Proceedings of the Japan-USA Symposium on Flexible Automation* (1994), p. 219.
- ²⁶N. D. Bhat, “Modeling and precision control of ionic polymer metal composite,” Master’s thesis (Texas A&M University, 2003).
- ²⁷R. Kanno, S. Tadokoro, T. Takamori, and M. Hattori, in *Proceedings of the IEEE International Conference on Robotics and Automation* (Minneapolis, MN, 1996), pp. 219–225.
- ²⁸K. M. Newbury and D. J. Leo, *J. Intell. Mater. Syst. Struct.* **14**, 333 (2003).
- ²⁹C. Bonomo, L. Fortuna, P. Giannone, S. Graziani, and S. Strazzeri, *Smart Mater. Struct.* **16**, 1 (2007).
- ³⁰P. G. de Gennes, K. Okumura, M. Shahinpoor, and K. Kim, *Europhys. Lett.* **50**, 513 (2000).
- ³¹S. Tadokoro, S. Yamagami, T. Takamori, and K. Oguro, *Proc. SPIE* **3987**, 92–102 (2000).
- ³²K. M. Farinholt, “Modeling and characterization of ionic polymer transducers for sensing and actuation,” Ph.D. dissertation (Virginia Polytechnic Institute and State University, 2005).
- ³³P. J. Costa Branco and J. A. Dente, *Smart Mater. Struct.* **15**, 378 (2006).
- ³⁴G. Del Bufalo, L. Placidi, and M. Porfiri, *Smart Mater. Struct.* **17**, 045010 (2008).

- ³⁵K. M. Newbury and D. J. Leo, *J. Intell. Mater. Syst. Struct.* **13**, 51 (2002).
- ³⁶Y. Bar-Cohen, X. Bao, S. Shrit, and S.-S. Lih, *Proc. SPIE* **4695**, 286–293 (2002).
- ³⁷J. W. Paquette, K. J. Kim, J.-D. Nam, and Y. S. Tak, *J. Intell. Mater. Syst. Struct.* **14**, 633 (2003).
- ³⁸Z. Chen, X. Tan, and M. Shahinpoor, in *Proceedings of the IEEE/ASME International Conference on Advanced Intelligent Mechatronics* (Monterey, CA, 2005), pp. 60–65.
- ³⁹L. Hao and Z. Li, *Smart Mater. Struct.* **19**, 025014 (2010).
- ⁴⁰C. S. Kothera and D. J. Leo, *J. Vib. Control* **11**, 519 (2005).
- ⁴¹C. S. Kothera, D. J. Leo, and S. L. Lacy, *J. Vib. Control* **14**, 1151 (2008).
- ⁴²T. Wallmersperger, D. Leo, and C. Kothera, *J. Appl. Phys.* **101**, 4912 (2007).
- ⁴³J. D. Davidson and N. C. Goulbourne, *J. Appl. Phys.* **109**, 084901 (2011).
- ⁴⁴Z. Chen, D. R. Hedgepeth, and X. Tan, *Smart Mater. Struct.* **18**, 055008 (2009).
- ⁴⁵Z. Chen and X. Tan, *IEEE/ASME Trans. Mechatron.* **13**, 519 (2008).
- ⁴⁶J. Ryu, S.-S. Kim, and S.-S. Kim, *Comput. Struct.* **62**, 1035 (1997).
- ⁴⁷D. C. D. Oguamanam, S. F. M. de Almeida, and J. S. Hansen, *J. Intell. Mater. Syst. Struct.* **9**, 137 (1998).
- ⁴⁸Y. Fang, T. J. Pence, and X. Tan, *Smart Mater. Struct.* **17**, 065020 (2008).